


Experimental Realization of a Deterministic Quantum Router with Superconducting Quantum Circuits

Zhiling Wang,[‡] Yukai Wu,[‡] Zenghui Bao, Yan Li[✉], Cheng Ma, Haiyan Wang, Yipu Song, Hongyi Zhang,^{*} and Luming Duan[†]

Center for Quantum Information, Institute for Interdisciplinary Information Sciences, Tsinghua University, Beijing 100084, People's Republic of China

 (Received 30 June 2020; revised 7 January 2021; accepted 11 January 2021; published 27 January 2021)

A quantum router is an elementary building block for quantum-information processing. It directs the incoming quantum signal to different routes with phase coherence. To realize scalable quantum routing, a single particle needs to deterministically and coherently route the paths of a flying qubit, which requires nonlinear interaction at the single quantum level and complicated path-data qubit control so far beyond the experimental reach. Here we demonstrate a deterministic quantum router working at microwave frequencies based on superconducting circuits, which can naturally integrate with a leading platform for quantum computing. We encode the quantum signal into a weak coherent pulse and use an entanglement witness to rigorously verify the generated entanglement between the control qubit and the path of the data qubit, thus proving quantum coherence of the routing operation. Our experiment lays the foundation for useful applications of quantum routers in quantum networks and quantum random-access memories.

DOI: [10.1103/PhysRevApplied.15.014049](https://doi.org/10.1103/PhysRevApplied.15.014049)

I. INTRODUCTION

A router is a key element in a classical communication network. It directs signals (data) to different destinations (paths) according to the address (control) information, and thus enables complex communication patterns in the network. Different from a classical router, a genuine quantum router has all the data, path, and control information represented by qubits [1]: the internal-data qubit state of the incoming signal is preserved after the routing process, while its outgoing path acquires quantum correlation with the control qubit and the control-path qubits are generally entangled. This requires strong nonlinear interaction between the control qubit and the signal, which is typically a flying photon pulse carrying both the data qubit and the path qubit.

Many theoretical and experimental efforts have been pursued towards a genuine quantum router. Previous experiments mainly explore the linear optical systems [2,3], where the required nonlinear interaction is generated by postselection in the coincidence basis; these implementations are thus probabilistic and not scalable. A deterministic quantum router is necessary for its scalable application in a quantum network [4], as well as for application in quantum random access memories (QRAMs)

[5] for potential exponential speedup of many quantum algorithms requiring parallel input of classical data [6–9]. Some theoretical proposals for deterministic quantum routers exist [10–12], but have not been demonstrated yet due to the experimental difficulty.

In this work, we demonstrate a deterministic quantum router using microwave photons as the signal and a superconducting transmon qubit as the control. The data qubit is frequency encoded in a weak coherent pulse. We measure the output on different paths and their quantum correlation with the control qubit through continuous-variable measurements. We develop an error model to estimate the fidelity of the control-path quantum state and prove the existence of entanglement using an entanglement witness. To characterize the preservation of the data qubit after quantum routing, we project the measured weak coherent pulse state onto the single-photon subspace to perform quantum-process tomography.

II. THE IMPLEMENTATION SCHEME

Our quantum router is shown schematically in Fig. 1(a). It consists of two cavities with frequencies ω_1 and ω_2 , each for one frequency component encoding the data qubit, coupled dispersively with a superconducting qubit (control qubit). The Hamiltonian of the system is [13] $H = \hbar(\omega_1 - \chi_1 |1\rangle_c \langle 1|_c) a_1^\dagger a_1 + \hbar(\omega_2 - \chi_2 |1\rangle_c \langle 1|_c) a_2^\dagger a_2 + \hbar\omega_q |1\rangle_c \langle 1|_c$, where a_1 and a_2 denote the annihilation operators of the two cavity modes, ω_q the frequency of the control qubit, χ_1 and χ_2 the dispersive

^{*}hyzhang2016@tsinghua.edu.cn

[†]lmduan@tsinghua.edu.cn

[‡]These authors contributed equally to this work.

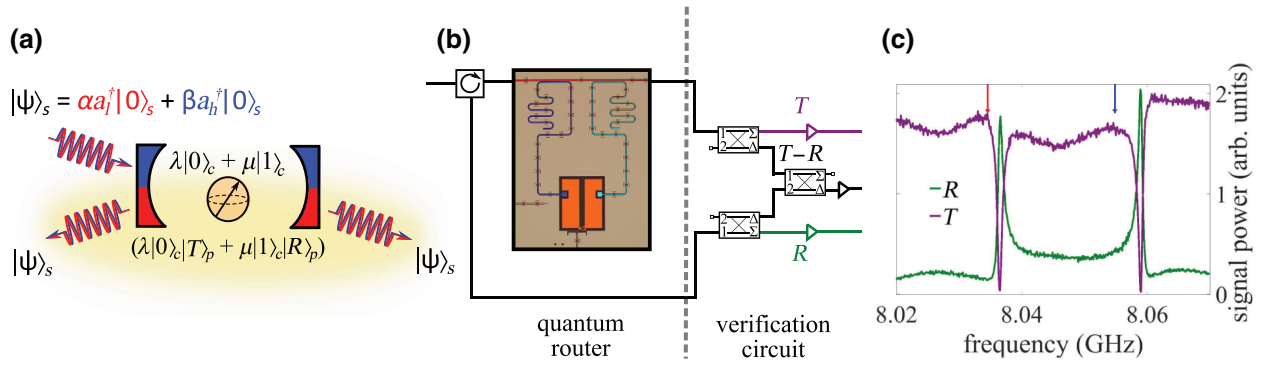


FIG. 1. Experimental setup and quantum router scheme. (a) Schematic of the proposed deterministic quantum router for microwave photons. A superconducting qubit (control qubit) is dispersively coupled with two cavities (red and blue) with different bare frequencies. An incident data qubit $|\psi\rangle_s$ frequency encoded in a single photon state (weak coherent pulse) either reflects back if its two frequency components are resonant with the two cavities, or goes through if off resonant. The control qubit can shift the frequency of the two cavities, and thus determine the output path of the signal. When the control qubit is set to $\lambda |0\rangle_c + \mu |1\rangle_c$, control-path entanglement will be generated after the routing operation and the ideal output state becomes $(\lambda |0\rangle_c |T\rangle_p + \mu |1\rangle_c |R\rangle_p) |\psi\rangle_s$. (b) Illustration of the experimental setup. On the chip (brown) two coplanar waveguide resonators (blue and green) are coupled with a transmon qubit (orange). The input signal is incident onto the resonators through a transmission line (red). The transmitted and the reflected (with the help of a circulator) signals are split and interfered by three microwave hybrid couplers (labeled with T , R and $T-R$) for the continuous-variable measurements. (c) The transmission and reflection spectra of the two CPW resonators for the control qubit in the ground state $|0\rangle_c$. The two frequency components of the data qubit are resonant with the two cavities when the transmon qubit is in the excited state $|1\rangle_c$ (red and blue arrows), and are shifted from resonance when in the ground state $|0\rangle_c$ (peaks and valleys in the spectra) through dispersive coupling.

coupling strength between the qubit and the two cavities. When the control qubit is in $|1\rangle_c$, the frequencies of the two cavities are shifted by χ_1 and χ_2 , respectively. Without loss of generality, we assume $\omega_1 < \omega_2$. We further design the cavities such that $\chi_1, \chi_2 \ll \omega_2 - \omega_1$. Experimentally we realize this setup by coupling two superconducting coplanar waveguide (CPW) resonators with a common transmon qubit, as shown in Fig. 1(b). The measured transmission and reflection spectra of the two cavities are shown in Fig. 1(c). An incoming photon pulse along the CPW transmission line can transmit through a cavity if it is far off resonant, while it will be reflected back when on resonance with the cavity [14]. Detailed parameters for the cavities and the transmon qubit can be found in Appendix B.

We can frequency encode the data qubit into a single-photon pulse [15] $|\psi\rangle_s = \alpha a_l^\dagger |0\rangle_s + \beta a_h^\dagger |0\rangle_s$, where l and h denote the low- and the high-frequency components at frequencies f_l and f_h . Now we choose $2\pi f_l = \omega_1 - \chi_1$ and $2\pi f_h = \omega_2 - \chi_2$. When the control qubit is in $|0\rangle_c$, both the incoming frequency components are off resonant with both the cavities, and thus the routed signal enters the transmission path, which we denote as $|T\rangle_p$. On the other hand, if the control qubit is in $|1\rangle_c$, the incoming frequency components will always be resonant with one of the two cavities and hence be reflected, which we denote as $|R\rangle_p$. Since both frequency components encoding the data qubit are transmitted or reflected in the same way, ideally the data qubit will be preserved with high fidelity and stays unrelated to the control and the path qubits. For arbitrary superposition state of the control qubit $\lambda |0\rangle_c + \mu |1\rangle_c$,

we thus obtain the ideal final state $|\Psi\rangle = (\lambda |0\rangle_c |T\rangle_p + \mu |1\rangle_c |R\rangle_p) |\psi\rangle_s$, as shown in Fig. 1(a).

In optical systems, such a single-photon pulse can be prepared and measured by single-photon generators and detectors. In the microwave range, we do not have such devices at hand with high quantum efficiency, therefore here we approximate the incoming single-photon state by a weak coherent pulse with average photon number below one, and measure the outgoing state through continuous-variable measurements, as was done in previous microwave experiments [16]. Since the above routing mechanism is not sensitive to the photon number, we still have a deterministic quantum router for the quantum signal.

III. ROUTING A WEAK COHERENT PULSE

To characterize the performance of the quantum router, first we focus on a single frequency component and study the entanglement of the control-path qubits. Ideally an incoming weak coherent pulse $|\alpha\rangle$ will be directed by a control qubit $\cos\theta |0\rangle_c + e^{i\phi} \sin\theta |1\rangle_c$ into the state $\cos\theta |0\rangle_c |\alpha\rangle_T |0\rangle_R + e^{i\phi} \sin\theta |1\rangle_c |0\rangle_T |\alpha\rangle_R$, where subscripts T and R represent coherent states on the transmitted and reflected paths. This would require infinite extinction ratios $r_T = P_{0T}/P_{1T}$ and $r_R = P_{1R}/P_{0R}$ of the system, where $P_{0(1)T(R)}$ is the output power on the path T (R) when the control qubit is set to $|0\rangle_c$ ($|1\rangle_c$). Under finite extinction ratio, a small fraction of the incoming pulse is routed to the wrong path, thus we assume that the actual

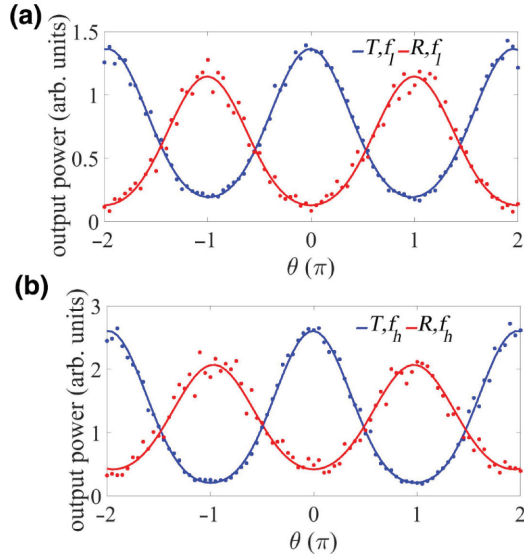


FIG. 2. Classical routing of weak coherent pulses. Blue and red data points are the output powers from the path T and the path R when rotating the polar angle θ in the control qubit state $\cos\theta |0\rangle_c + \sin\theta |1\rangle_c$. The quantum state of the input signal is set to (a) the low frequency f_l and (b) the high frequency f_h , with an average photon number of 0.35. The curves are corresponding fitting results with a squared sinusoidal model.

quantum state takes the form

$$\cos\theta |0\rangle_c |\alpha_0^T\rangle_T |\alpha_0^R\rangle_R + e^{i\phi} \sin\theta |1\rangle_c |\alpha_1^T\rangle_T |\alpha_1^R\rangle_R, \quad (1)$$

plus a possible phase noise between the two basis states. These parameters can be calibrated by measuring the ratio of voltages on each output port and a photon-number-dependent phase shift of the control qubit (see Appendix C for details).

The classical correlation between the control and the path qubits is characterized by the oscillation of average photon numbers in the paths T and R when scanning θ , as shown in Fig. 2. The measured curves match reasonably well with the ideal sinusoidal oscillation predicted by Eq. (1), and the deviation can be from statistical errors and noise in the amplifiers. Here the input signal with an average photon number of 0.35 is shaped to a square pulse with a duration of $2\ \mu\text{s}$, which well fits the bandwidth of the cavities. For an input signal at the low frequency f_l , the measured extinction ratio is about $r_T = 8.5\ \text{dB}$ and $r_R = 9.5\ \text{dB}$, while for a signal at the high frequency f_h the extinction ratio is about $r_T = 11.3\ \text{dB}$ and $r_R = 6.8\ \text{dB}$.

IV. CONTROL-PATH CORRELATION AND ENTANGLEMENT

We further characterize the phase noise in Eq. (1) through the interference between the two paths. As shown in Fig. 1(b), we use two microwave hybrid couplers to direct half of the transmitted and reflected signals to the

third one and mix them together into a path $T - R$ (signal in the other path $T + R$ is discarded). We prepare the control qubit in equal superposition of the two basis states $(|0\rangle_c + e^{i\phi} |1\rangle_c)/\sqrt{2}$ and send the signal pulse through the quantum router. By projecting the control qubit to $(|0\rangle_c \pm |1\rangle_c)/\sqrt{2}$, we achieve interference between the two paths:

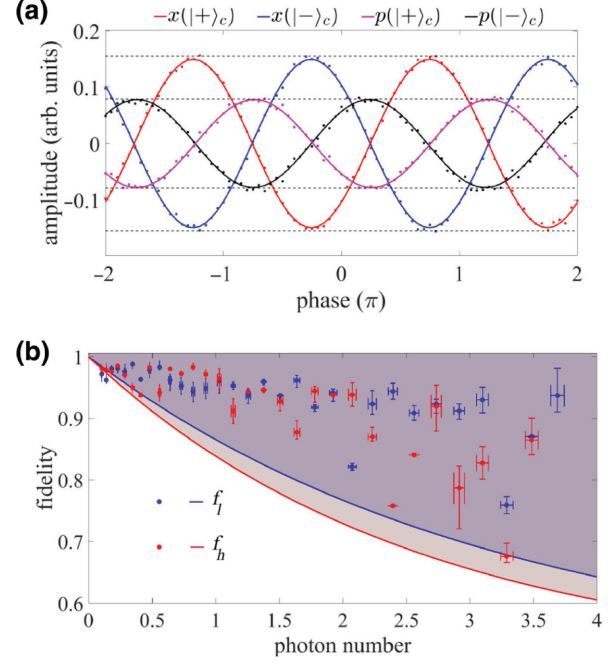


FIG. 3. Control-path correlation and entanglement. (a) The measured x and p quadratures of the signal field from the path $T - R$ when the control qubit is projected to $|\pm\rangle_c = (|0\rangle_c \pm |1\rangle_c)/\sqrt{2}$, which show oscillations when sweeping the azimuthal angle ϕ of the initial control qubit state $(|0\rangle_c + e^{i\phi} |1\rangle_c)/\sqrt{2}$. The solid lines are fitting results with the $\cos\phi$ model. The dash lines indicate the theoretical amplitude from the calibrated experimental parameters. With any of the four oscillations, $x(|+\rangle_c)$, $x(|-\rangle_c)$, $p(|+\rangle_c)$, and $p(|-\rangle_c)$, the fidelity from the theoretical state $|\psi\rangle = (|0\rangle_c |\alpha_0^T\rangle_T |\alpha_0^R\rangle_R + e^{i\phi} |1\rangle_c |\alpha_1^T\rangle_T |\alpha_1^R\rangle_R)/\sqrt{2}$ can be learnt using the ratio of the measured oscillation amplitude to the corresponding theoretical value. We take the average value as the state fidelity F . See Appendix D for more details. Here the input signal is at the low frequency f_l with an average photon number $\bar{n} = 0.4$. (b) The blue and the red data points are the fidelity F for the low-frequency f_l and the high-frequency f_h components, respectively. The vertical error bars are given by the minimum and maximum value of the four ratios described in (a). The horizontal error bars are given by the standard deviation in calibrating the average photon number. We use an entanglement witness to verify the existence of quantum entanglement between the path and the control qubits. The solid lines show the entanglement threshold above which the system must be entangled. Here we vary \bar{n} from 0 to 4. For most cases the measured fidelity is well above the entanglement threshold, and thus proves a genuine quantum router. Note that although the protocol requires low average photon number to approximate a single-photon state, we can prove entanglement for a much wider range of \bar{n} .

the two quadratures $x = (a^\dagger + a)/2$ and $p = i(a^\dagger - a)/2$ of the signal field in the path $T - R$ will oscillate with ϕ [see Fig. 3(a), more details can be found in Appendix D]. The existence of phase error in Eq. (1) reduces the oscillation amplitude from the ideal case. By comparing the measured oscillation amplitude with the theoretical value from the calibrated experimental parameters, we obtain a fidelity due to the phase noise, as shown in Fig. 3(b).

Given the above results, we can hypothetically project the final state into the single-photon subspace and compute an entanglement fidelity for the control-path qubits. Following the calculation in Appendix D, we obtain $F_e = 0.865$ above the entanglement criteria of 0.5. However, since we are not experimentally equipped with a microwave single-photon detector, it is desirable to directly prove the existence of entanglement in the control-path subsystem, which is a key feature for a genuine quantum router. Here the difficulty is that the coherent pulses with small average photon number are not orthogonal to each other even in the ideal case. To verify entanglement, we utilize an entanglement witness [17] $W = \beta I - |\psi\rangle\langle\psi|$ with $|\psi\rangle = (|0\rangle_c |\alpha_0^T\rangle_T |\alpha_0^R\rangle_R + |1\rangle_c |\alpha_1^T\rangle_T |\alpha_1^R\rangle_R)/\sqrt{2}$. The choice of β should ensure that $\text{tr}[W\rho_{\text{sep}}] \geq 0$ for any separable state ρ_{sep} between the control qubit and the path; thus $\text{tr}[W\rho] < 0$ verifies the entanglement. As is mentioned above, since the two path states $|T\rangle = |\alpha_0^T\rangle_T |\alpha_0^R\rangle_R$ and $|R\rangle = |\alpha_1^T\rangle_T |\alpha_1^R\rangle_R$ are not orthogonal, we can choose $\beta = (1 + |\langle T|R\rangle|)/2$ (see Appendix D for more details) [18]. When characterizing the phase noise, we measure a fidelity F between the actual quantum state and the theoretical state $|\psi\rangle$. By comparing it with β from the calibrated experimental parameters, we verify the entanglement in the control-path subsystem, as shown in Fig. 3(b). The blue and red solid lines indicate the entanglement threshold β as a function of average photon number \bar{n} for input states at the low frequency f_l and the high frequency f_h , respectively. The scattered points are the measured fidelity between the actual state ρ and the theoretical state $|\psi\rangle$. As we can see, for most of the cases the fidelity is larger than the corresponding threshold, which means $\text{tr}[W\rho] < 0$ and the existence of quantum entanglement. Note that although for the correct encoding of the data qubit we need to use a weak coherent pulse with low average photon number, we can verify entanglement for a wide range of average photon numbers. The measured fidelity does not change significantly with \bar{n} , while the threshold β to verify entanglement goes to 1 as $\bar{n} \rightarrow 0$ because it is difficult to distinguish very weak coherent pulses from each other due to the large overlap in their vacuum part.

V. QUANTUM PROCESS TOMOGRAPHY

Finally, we consider the fidelity of the routed data qubit. An ideal quantum router directs the input signal to the aimed path without changing its internal quantum state.

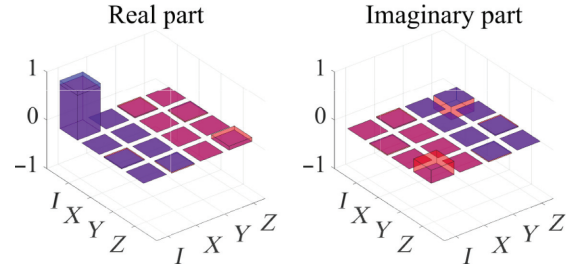


FIG. 4. Quantum-process tomography for the data qubit. We virtually project the experimentally calibrated output state [Eq. (1) with phase noise] to the single-photon subspace and perform quantum-process tomography [19,20]. Real and imaginary parts of the reconstructed process matrix are presented when the control qubit is in $|+\rangle_c = (|0\rangle_c + |1\rangle_c)/\sqrt{2}$ for the output signal from path R , with an average gate fidelity $\bar{F} = 0.973$. In the ideal case the quantum router well preserve the input quantum state, which is equivalent to an identity operation after normalization. The corresponding ideal matrix elements are indicated with the blue hollow caps. The case when the control qubit is in $|+\rangle_c (|1\rangle_c)$ and the output is from path $T (R)$ are shown in Appendix E with higher fidelities.

Therefore the routing process should be an identity gate in the subspace of the data qubit. To verify this, we should reconstruct the quantum channel of the routing process via quantum-process tomography [19,20]. Since we have already built the error model for the output state and have calibrated the experimental parameters, here we can directly extract the process fidelity by virtually projecting to the single-photon subspace (see more details in Appendix E). In Fig. 4 we show the reconstructed process matrix elements for the path R when the control qubit is set to $(|0\rangle_c + |1\rangle_c)/\sqrt{2}$, with a process fidelity $F_p = 0.960$. This corresponds to an average gate fidelity [20] $\bar{F} = 0.973$. For the control qubit at $(|0\rangle_c + |1\rangle_c)/\sqrt{2}$ and the signal on the path T , we similarly get a process fidelity $F_p = 0.962$ with the corresponding average gate fidelity $\bar{F} = 0.975$.

VI. DISCUSSION AND CONCLUSION

For our quantum router, the dominant error source is the photon leakage between the T and R modes due to the finite extinction ratio. It routes the data qubit into the wrong path and thus reduces the fidelity of the control-path entanglement. Furthermore, under the finite extinction ratio, the asymmetry in the response of the two cavities can distort the relative amplitudes of the two frequency components and thus lower the data qubit fidelity. The second useful error source is the phase noise in the superposition state given by Eq. (1), mainly due to the dephasing of the control qubit when the signal photon goes through. Here we assume that the system stays in the two-dimensional subspace spanned by $|0\rangle_c |\alpha_0^T\rangle_T |\alpha_0^R\rangle_R$ and $|1\rangle_c |\alpha_1^T\rangle_T |\alpha_1^R\rangle_R$.

This is a reasonable assumption because the reflection and transmission coefficients of the cavity is stable during the experiment. Also note that there is a delay between the routing of the quantum signal and the measurement of the control qubit, which leads to further dephasing of the final quantum state. Since this effect is not related to the functioning of the quantum router, we correct it using the measured coherence time of the control qubit, as discussed in Appendix F.

In summary, we demonstrate a deterministic quantum router for a frequency-encoded dual-rail microwave photonic qubit. By modeling the dominant source of errors, we characterize the performance of the device and rigorously prove the existence of control-path entanglement, a crucial feature for its application in quantum networks and QRAMs. With the microwave single-photon generators [21,22] and detectors [23–25] under development as well as suitable generalization of the frequency-encoded photonic qubits from the optical regime [15] to the microwave regime, the required encoding for the data qubit can be realized. The prototype quantum router demonstrated here has a compact design and can be scaled to a device with multiple input-output ports or for cascaded routing operations [10,26,27].

ACKNOWLEDGMENTS

This work is supported by the National Key Research and Development Program of China (Grant No. 2016YFA0301902), the Frontier Science Center for Quantum Information of the Ministry of Education of China, and the Tsinghua University Initiative Scientific Research Program. Y.K.W. acknowledges support from Shuimu Tsinghua Scholar Program and the International Postdoctoral Exchange Fellowship Program.

APPENDIX A: EXPERIMENTAL SETUP

Our sample is made from an aluminum film on a $7 \times 7 \text{ mm}^2$ sapphire substrate. The Josephson junction of the transmon qubit is made by $\text{Al}/\text{AlO}_x/\text{Al}$. The sample is wire bonded onto a PCB board in an aluminium sample box and cooled to $T \sim 14 \text{ mK}$ by a dilution refrigerator. The measurement setup is illustrated in Fig. 5

The continuous-wave carrier signal from the microwave signal generator is modulated at an IQ mixer with a low-frequency signal, which is produced by an arbitrary wave generator (AWG) with 1-GHz sampling rate. Such microwave pulses with tunable frequencies, amplitudes,

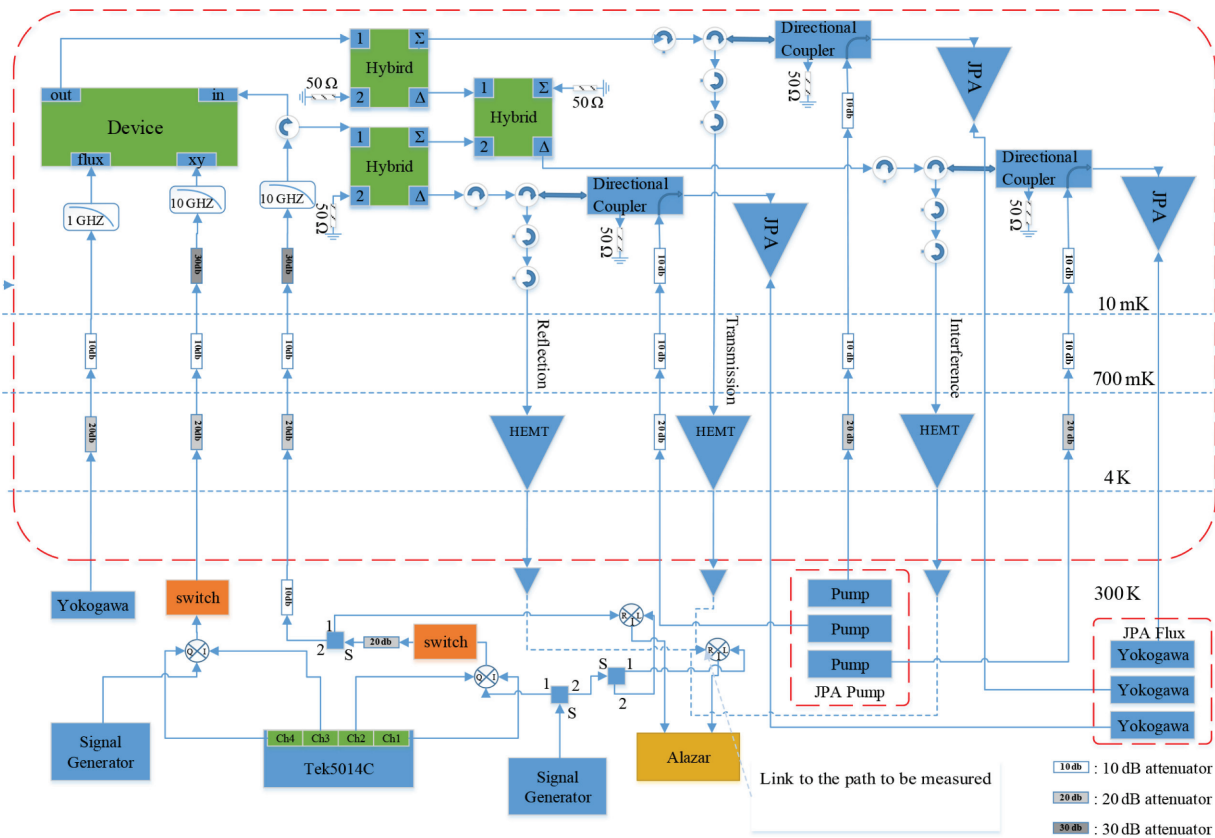


FIG. 5. Schematic of the experimental setup.

and phases can be used as the input signal (weak coherent pulse), the control qubit driving pulse and the qubit state readout pulse. The microwave pulses are attenuated and filtered to suppress the thermal noise and then are sent to the sample. Before the signal pulse enters the sample, a circulator is inserted to measure the reflected signal. In order to carry out the continuous-variable measurements in two different bases, the transmitted and reflected signals are first sent to two 3-dB 180° hybrid couplers (Krytar, 6–20 GHz) to split each signal into two paths Δ and Σ . The other two input ports of the two hybrids are terminated by 50- Ω resistors (see Fig. 5). The scattering matrix of an ideal 180° hybrid coupler can be written as [28]

$$[S_{mn}] = \frac{-i}{\sqrt{2}} \times \begin{bmatrix} 0 & 0 & 1 & 1 \\ 0 & 0 & 1 & -1 \\ 1 & 1 & 0 & 0 \\ 1 & -1 & 0 & 0 \end{bmatrix}, \quad (\text{A1})$$

where the subindices m and n take 1, 2, 3, 4, representing ports 1, 2, Σ , and Δ , respectively. The 50- Ω terminal provides an input of a thermal state. Since the base temperature is much lower than the GHz energy scale considered in the experiment, the thermal input can be approximated as a vacuum state, so the transmission and reflection hybrids work as a power divider. Output from Σ ports of the transmission and reflection hybrids are directly sent to the amplification chains and recorded as signal output from path T and path R , respectively. Output from Δ ports of the transmission and reflection hybrids are sent to another 180° hybrid for interference. According to Eq. A1, one would expect the output in the form of $\left| (T - R)/\sqrt{2} \right\rangle_p$ from Δ port and $\left| (T + R)/\sqrt{2} \right\rangle_p$ from Σ port. In our experiment we terminate the Σ port of the interference hybrid and send the output signal from the Δ port to the amplification chain, therefore the amplified $\left| (T - R)/\sqrt{2} \right\rangle_p$ state is recorded.

In the amplification chain, signal output from paths T , R , and $T - R$ are sent to three Josephson parametric amplifiers (JPA) separately to measured very weak signals at single-photon level and to perform single-shot readout for the state of the control qubit. We use two circulators between the hybrid couplers and the JPA to protect the qubit coherence from the amplified vacuum fluctuation generated by the JPA. The amplified signal is sent to two isolators mounted at the base plate, which are used to block the backward signal from following circuits. Then the signal is further amplified by a HEMT amplifier mounted on a 4-K plate and two microwave amplifiers at room temperature. The output signal is demodulated by a mixer to an intermediate frequency (IF) lower than 100 MHz and amplified by a fast preamplifier before entering into an analog-to-digital converter (ADC) with 1-GHz sampling

TABLE I. System parameters.

Frequency of cavity 1	$\omega_1/2\pi$ (GHz)	8.0364
Frequency of cavity 2	$\omega_2/2\pi$ (GHz)	8.0589
Qubit resonant frequency	$\omega_q/2\pi$ (GHz)	5.9
Out-coupling quality factor of cavity 1	Q_c^1	9500
Out-coupling quality factor of cavity 2	Q_c^2	10560
Internal quality factor of cavity 1	Q_i^1	6×10^5
Internal quality factor of cavity 2	Q_i^2	9.5×10^5
Decay rate of cavity 1	$\kappa_1/2\pi$ (MHz)	0.98
Decay rate of cavity 2	$\kappa_2/2\pi$ (MHz)	0.8
Dispersive shift of cavity 1	$\chi_1/2\pi$ (MHz)	1.14
Dispersive shift of cavity 1	$\chi_2/2\pi$ (MHz)	2.81
Qubit relaxation time	T_1 (μs)	5.5
Qubit dephasing time	T_2 (μs)	4.5
Qubit dephasing time (echo)	T_2^e (μs)	4.5
JPA gain for transmission path	G_T	21 dB
JPA gain for reflection path	G_R	14 dB
JPA gain for interference path	G_{T-R}	22 dB

rate. A reference signal without entering into the refrigerator is used as the phase reference of the signal from the sample. The in-phase and quadrature signals are then extracted with a digital homodyne method. Some parameters of the sample and the measurement system are listed in Table I.

In the experiment, the well-calibrated DRAG (Derivative Removal via Adiabatic Gate) pulses with the length of 20 ns are used to set the state of the control qubit. A square pulse with the length of 1 μs is used for qubit-state readout. The qubit state can be determined in a single shot on paths T , R , and $T - R$ with the help of the JPAs. The input signal $|\psi\rangle_s$ to be routed is also shaped to a square pulse with the duration of 2 μs to fit the bandwidth of the cavities. Since it is typically very weak (on the single-photon level), the output signal from the router has to be averaged by 10^5 trails to obtain the output quadratures with satisfactory signal-to-noise ratio.

APPENDIX B: TRANSMISSION AND REFLECTION COEFFICIENTS OF THE CAVITY

As one of the core components of the quantum router, the spectra of the CPW cavities largely determine the performance of the router. The transmission and the reflection

spectra for a hanger cavity are given by [29]

$$\begin{aligned} t(f) &= 1 - \frac{Q_r/Q_c}{1 + 2iQ_r(f - f_0)/f_0}, \\ r(f) &= -\frac{Q_r/Q_c}{1 + 2iQ_r(f - f_0)/f_0}, \end{aligned} \quad (\text{B1})$$

where Q_r , Q_c , and Q_i are the loaded quality factor, out-coupling quality factor, and internal quality factor, respectively, with $1/Q_r = 1/Q_c + 1/Q_i$. f_0 is the resonance frequency of one of the two cavities, which is further controlled by a transmon qubit through the dispersive coupling.

As described in the main text, we set the signal frequency f to the resonance frequency of the cavity f_0 when the control qubit is in the excited state $|1\rangle_c$. In this case, the input signal would be largely reflected by the cavity and directed to the reflection path with a reflection coefficient $|r(f_0)| = Q_r/Q_c$ and a transmission coefficient $|t(f_0)| = 1 - Q_r/Q_c = Q_r/Q_i$, as predicted by Eq. (B1). When the control qubit is prepared in the ground state $|0\rangle_c$, we would have $f = f_0 - \chi$ and the input signal would largely transmit through the cavity and be directed to the transmission path. We get $|r(f_0 - \chi)| = |Q_r/Q_c/(1 - 2iQ_r\chi/f_0)|$ and $|t(f_0 - \chi)| = |1 - Q_r/Q_c/(1 - 2iQ_r\chi/f_0)|$.

The extinction ratio on the reflection path is defined as $r_e^R = 20 \log_{10}[|r(f_0)|/|r(f_0 - \chi)|] = 10 \log_{10}(1 + A^2)$, where $A^2 = (2Q_r\chi/f_0)^2 \gg 1$. Therefore, large χ and Q_r are preferred for a high extinction ratio. On the transmission path, $r_e^T = 20 \log_{10}[|t(f_0 - \chi)|/|t(f_0)|] \approx 20 \log_{10}(Q_i/Q_r)$. A large Q_i compared with Q_c is thus preferred to get a high extinction ratio. According to the parameters listed in Table I, the predicted extinction ratios on the reflection path and transmission path are better than 30 dB for both the low-frequency f_l and the high-frequency f_h modes.

The measured extinction ratios are considerably smaller than those of the predicted ones due to the following reasons: first, the spurious modes of the microwave circuit introduce background signal to the measured transmission and reflection spectra; second, the impedance mismatch at the input port results in unwanted signal reflection before entering the device (about 8%), such that the output from the reflection path cannot be effectively turned off. This could be alleviated by improving the bonding between the chip and microwave connections.

It should be noted that the router suffers from signal loss when the signal frequency is on resonance with the cavity, due to the nonzero internal loss rate. When $f = f_0$, we can get the loss ratio r between the total output power and the input power by

$$r = |t(f_0)|^2 + |r(f_0)|^2 = 1 - \frac{2Q_r}{Q_c} + \frac{2Q_r^2}{Q_c^2}. \quad (\text{B2})$$

In our device we have a loss ratio r of about 0.95 for the low-frequency mode $|f_l\rangle$ and 0.97 for the high-frequency mode $|f_h\rangle$.

APPENDIX C: QUANTUM STATES ON OUTPUT PATHS

In this section, we study the output quantum states of the router when the control qubit is prepared at $(|0\rangle_c + e^{i\phi}|1\rangle_c)/\sqrt{2}$ and the incoming pulse is a weak coherent state. We give analytical expressions for the probability to measure the control qubit in the $|+\rangle_c$, $|-\rangle_c$ basis and the corresponding average voltage in the output ports. These results can help us to characterize the performance of the quantum router in the following sections.

1. Ideal case

Consider an input pulse as a coherent state $|\alpha\rangle$, which can be at the low frequency f_l or the high frequency f_h encoding the data qubit. Ideally, if the control qubit is in $|0\rangle_c$ ($|1\rangle_c$), the input signal will be completely transmitted (reflected). Thus if we prepare the control qubit at $(|0\rangle_c + e^{i\phi}|1\rangle_c)/\sqrt{2}$, the ideal output state of the quantum router will be

$$\frac{1}{\sqrt{2}} (|0\rangle_c |\alpha\rangle_T |0\rangle_R + e^{i\phi} |1\rangle_c |0\rangle_T |\alpha\rangle_R), \quad (\text{C1})$$

where the subscripts c , T , and R correspond to the control qubit and the coherent pulses in the transmitted and reflected paths.

As shown in Fig. 1(b) of the main text, half of the output pulses from T and R will be delivered to a microwave hybrid coupler for interference. Then the quantum state becomes

$$\begin{aligned} &\frac{1}{\sqrt{2}} |0\rangle_c \left| \frac{\alpha}{\sqrt{2}} \right\rangle_T |0\rangle_R \left| \frac{\alpha}{2} \right\rangle_+ \left| \frac{\alpha}{2} \right\rangle_- \\ &+ \frac{1}{\sqrt{2}} e^{i\phi} |1\rangle_c |0\rangle_T \left| \frac{\alpha}{\sqrt{2}} \right\rangle_R \left| \frac{\alpha}{2} \right\rangle_+ \left| -\frac{\alpha}{2} \right\rangle_-, \end{aligned} \quad (\text{C2})$$

where $+$ and $-$ represent the $(T + R)/\sqrt{2}$ and $(T - R)/\sqrt{2}$ modes. Note that in our experiment the $+$ mode is not used.

Now if we project the control qubit to the $|\pm\rangle_c = (|0\rangle_c \pm |1\rangle_c)/\sqrt{2}$ basis, the corresponding unnormalized quantum state for the outgoing microwave photons will be

$$\begin{aligned} |\Psi_{\text{ph},\pm}^{(\text{ideal})}\rangle &= \frac{1}{2} \left(\left| \frac{\alpha}{\sqrt{2}} \right\rangle_T |0\rangle_R \left| \frac{\alpha}{2} \right\rangle_+ \left| \frac{\alpha}{2} \right\rangle_- \right. \\ &\quad \left. \pm e^{i\phi} |0\rangle_T \left| \frac{\alpha}{\sqrt{2}} \right\rangle_R \left| \frac{\alpha}{2} \right\rangle_+ \left| -\frac{\alpha}{2} \right\rangle_- \right). \end{aligned} \quad (\text{C3})$$

The success probability of this projection measurement is thus given by

$$P_{\pm} = \left\langle \Psi_{\text{ph},\pm}^{(\text{ideal})} \middle| \Psi_{\text{ph},\pm}^{(\text{ideal})} \right\rangle = \frac{1}{2} \left(1 \pm e^{-|\alpha|^2} \cos \phi \right) = \frac{1}{2} \left(1 \pm e^{-N} \cos \phi \right), \quad (\text{C4})$$

where $N = |\alpha|^2$ is the incoming photon number. The expectation value of the annihilation operator in the $-$ mode conditioned on a successful projection measurement of the control qubit in the $|+\rangle_c$ ($|-\rangle_c$) state is

$$A_{\pm} = \frac{\left\langle \Psi_{\text{ph},\pm}^{(\text{ideal})} \middle| a_- \middle| \Psi_{\text{ph},\pm}^{(\text{ideal})} \right\rangle}{\left\langle \Psi_{\text{ph},\pm}^{(\text{ideal})} \middle| \Psi_{\text{ph},\pm}^{(\text{ideal})} \right\rangle} = \frac{\mp i \alpha e^{-|\alpha|^2} \sin \phi}{2(1 \pm e^{-|\alpha|^2} \cos \phi)}. \quad (\text{C5})$$

By varying ϕ , we shall be able to observe oscillations in P_{\pm} and A_{\pm} , which characterize the quantum coherence between the two paths T and R .

2. Quantum states under finite extinction ratio

As mentioned in the main text and in Appendix B, the performance of the real device deviates from the ideal case due to a finite extinction ratio. This can be described by a state analog to Eq. (C1):

$$\frac{1}{\sqrt{2}} \left(|0\rangle_c |\alpha_0^T\rangle_T |\alpha_0^R\rangle_R + e^{i\phi} |1\rangle_c |\alpha_1^T\rangle_T |\alpha_1^R\rangle_R \right). \quad (\text{C6})$$

After passing through the microwave hybrid couplers, the state becomes

$$|\Psi\rangle = \frac{1}{\sqrt{2}} \left(|0\rangle_c \left| \frac{\alpha_0^T}{\sqrt{2}} \right\rangle_T \left| \frac{\alpha_0^R}{\sqrt{2}} \right\rangle_R \left| \frac{\alpha_0^T + e^{i\theta_{RT}} \alpha_0^R}{2} \right\rangle_+ \right. \\ \times \left. \left| \frac{\alpha_0^T - e^{i\theta_{RT}} \alpha_0^R}{2} \right\rangle_- + e^{i\phi} |1\rangle_c \left| \frac{\alpha_1^T}{\sqrt{2}} \right\rangle_T \left| \frac{\alpha_1^R}{\sqrt{2}} \right\rangle_R \right. \\ \times \left. \left| \frac{\alpha_1^T + e^{i\theta_{RT}} \alpha_1^R}{2} \right\rangle_+ \left| \frac{\alpha_1^T - e^{i\theta_{RT}} \alpha_1^R}{2} \right\rangle_- \right), \quad (\text{C7})$$

where θ_{RT} characterizes the phase difference between the T and R modes due to the imbalanced circuit lengths, when they are interfered at the third hybrid coupler.

Following the similar derivations as the ideal case, we find the success probability to project the control qubit to the $|\pm\rangle_c$ states as

$$P_{\pm} = \frac{1}{2} [1 \pm C \cos(\phi + \delta)], \quad (\text{C8})$$

where

$$C = \exp \left[-\frac{1}{2} (|\alpha_0^T|^2 + |\alpha_0^R|^2 + |\alpha_1^T|^2 + |\alpha_1^R|^2) \right. \\ \left. + \text{Re} (\alpha_0^{T*} \alpha_1^T + \alpha_0^{R*} \alpha_1^R) \right], \quad (\text{C9})$$

and

$$\delta = \text{Im} (\alpha_0^{T*} \alpha_1^T + \alpha_0^{R*} \alpha_1^R). \quad (\text{C10})$$

The conditioned average amplitude in the $-$ mode when the control qubit is in $|\pm\rangle_c$ reads

$$A_{\pm} = \frac{1}{2\sqrt{2}} \frac{(\alpha_0^- + \alpha_1^-) \pm C [\alpha_0^- e^{-i(\phi+\delta)} + \alpha_1^- e^{i(\phi+\delta)}]}{1 \pm C \cos(\phi + \delta)}, \quad (\text{C11})$$

where we define

$$\alpha_{0(1)}^- = \frac{\alpha_{0(1)}^T - e^{i\theta_{RT}} \alpha_{0(1)}^R}{\sqrt{2}}. \quad (\text{C12})$$

Both the real and the imaginary parts of A_{\pm} oscillate with ϕ .

3. Calibration of experimental state

The parameters for the quantum state at the output ports cannot be measured directly, because the amplification factors and the circuit lengths for all the output modes are not identical. However, we can reasonably assume that the signal from a given mode has the same amplification and phase shift regardless of the control qubit state. Here we describe how we calibrate the output quantum state based on the experimentally measurable quantities.

For an input signal with an average photon number of N , the following equations shall be satisfied due to the conservation of energy

$$|\alpha_0^T|^2 + |\alpha_0^R|^2 = N, \quad (\text{C13}) \\ |\alpha_1^T|^2 + |\alpha_1^R|^2 = rN,$$

where the factor r is introduced in Eq. (B2) due to the internal loss of the cavity.

Since the amplification factors for signals on the paths T and R may not be identical, we consider the ratio of the signal amplitudes on each path

$$\gamma_T = \alpha_1^T / \alpha_0^T, \quad (\text{C14}) \\ \gamma_R = \alpha_0^R / \alpha_1^R.$$

γ_T and γ_R are complex numbers, which contain both the magnitude and phase information. Ideally both values will be zero. They can be measured in the experiment by comparing the output amplitudes in the T and R modes when the control qubit is set to $|0\rangle_c$ and $|1\rangle_c$.

Solving the above equations we find

$$\begin{aligned}
\alpha_0^T &= \sqrt{N} \sqrt{\frac{1 - r|\gamma_R|^2}{1 - |\gamma_T\gamma_R|^2}}, \\
\alpha_1^T &= \gamma_T \sqrt{N} \sqrt{\frac{1 - r|\gamma_R|^2}{1 - |\gamma_T\gamma_R|^2}}, \\
\alpha_0^R &= \gamma_R \sqrt{N} \sqrt{\frac{r - |\gamma_T|^2}{1 - |\gamma_T\gamma_R|^2}}, \\
\alpha_1^R &= \sqrt{N} \sqrt{\frac{r - |\gamma_T|^2}{1 - |\gamma_T\gamma_R|^2}}.
\end{aligned} \tag{C15}$$

Two of the relative phases among these four amplitudes are fixed by γ_T and γ_R , and the remaining one can be absorbed into θ_{RT} in Eq. (C7) when the T and R modes are interfered together.

Plugging these expressions into the definition of $\alpha_{0(1)}^-$, we have

$$\begin{aligned}
\alpha_0^- &= \frac{\alpha_0^T - e^{i\theta_{RT}} \alpha_0^R}{\sqrt{2}} \\
&= \sqrt{\frac{N}{2}} \left(\sqrt{\frac{1 - r|\gamma_R|^2}{1 - |\gamma_T\gamma_R|^2}} - \gamma_R e^{i\theta_{RT}} \sqrt{\frac{r - |\gamma_T|^2}{1 - |\gamma_T\gamma_R|^2}} \right), \\
\alpha_1^- &= \frac{\alpha_1^T - e^{i\theta_{RT}} \alpha_1^R}{\sqrt{2}} \\
&= \sqrt{\frac{N}{2}} \left(\gamma_T \sqrt{\frac{1 - r|\gamma_R|^2}{1 - |\gamma_T\gamma_R|^2}} - e^{i\theta_{RT}} \sqrt{\frac{r - |\gamma_T|^2}{1 - |\gamma_T\gamma_R|^2}} \right).
\end{aligned} \tag{C16}$$

We can also directly measure the ratio of the amplitudes on the $-$ mode $\gamma_- = \alpha_1^-/\alpha_0^-$ when the control qubit is at $|0\rangle_c$ and $|1\rangle_c$. Combining these results, we finally reach an expression for θ_{RT} :

$$\exp(i\theta_{RT}) = \frac{\gamma_- \alpha_0^T - \alpha_1^T}{\gamma_- \alpha_0^R - \alpha_1^R} = \frac{(-\gamma_- + \gamma_T) \sqrt{1 - r|\gamma_R|^2}}{(1 - \gamma_- \gamma_R) \sqrt{r - |\gamma_T|^2}}. \tag{C17}$$

In the experiment, we first set the control qubit in either $|0\rangle_c$ or $|1\rangle_c$, then send the input signal to the router with certain average photon numbers. The in-phase and quadrature components of the output signal from paths T , R , and $T - R$ are averaged and recorded. For either $|0\rangle_c$ state or $|1\rangle_c$ state the measurements are repeated for 40 times to reduce statistical errors. The averaged results give $\alpha_{0(1)}^T$, $\alpha_{0(1)}^R$, and $\alpha_{0(1)}^-$, from which γ_R , γ_T , and γ_- can be deduced from their definitions.

For low-frequency component $|f_l\rangle$ we measure $\gamma_{T,L} = 0.38e^{-0.72i}$, $\gamma_{R,L} = 0.33e^{0.98i}$, $\gamma_{-,L} = 1.11e^{0.79i}$, and $r_L = 0.95$. Thus we obtain $\theta_{RT,L} = -1.74 + 0.0023i$. For the high-frequency component $|f_h\rangle$ we have $\gamma_{T,H} = 0.27e^{-2.65i}$, $\gamma_{R,H} = 0.45e^{-1.17i}$, $\gamma_{-,H} = 0.79e^{2.46i}$, and $r_H = 0.97$, hence $\theta_{RT,H} = -0.49 - 0.0033i$. Note that the measured $\theta_{RT,L}$ and $\theta_{RT,H}$ are not exactly real numbers. The imaginary part represents the amplitude imbalance between signals from the T and R modes before interference, which could be induced by the imbalance of the hybrid coupler or the different circuit losses between the two paths. Nevertheless, the imaginary part of θ_{RT} is small and does not dominate our experimental errors. Therefore, we neglect it in our analysis.

Finally, we need to calibrate the average photon number N to recover the output state in Eq. (C7). Here we exploit Eq. (C8). As we can see, when we scan the azimuthal angle ϕ of the control qubit on the Bloch sphere, the probability for the final projection measurement on the $|\pm\rangle_c$ states oscillates as a cosine function, whose phase is shifted by δ [Eq. (C10)] compared with ϕ . This phase shift depends on the average photon number N of the input pulse. Specifically, we have

$$\delta = \frac{\text{Im}[\gamma_T(1 - \gamma_T^* \gamma_R^*) + r\gamma_R^*(1 - \gamma_T\gamma_R)]}{1 - |\gamma_R^2 \gamma_T^2|} N \tag{C18}$$

In the experiment we set the control qubit in $(|0\rangle_c + e^{i\phi}|1\rangle_c)/\sqrt{2}$ and send the input signal to the router with varied average photon numbers, and then perform projection measurement of the control qubit in the $|\pm\rangle_c$ basis. The measured state population are normalized to $[0, 1]$ for comparison, as shown in Figs. 6(a) and 6(b). We can see clear phase shifts when varying input signal powers. We then plot the phase shift versus the input power in Fig. 6(c). It can be seen that the phase shift is linearly dependent on the input photon number, as predicted in Eq. (C18). Here we fit the qubit phase shift to the power of the input signal, and compare the slope of the fitting with Eq. (C18) to obtain the incoming photon number N from its power.

APPENDIX D: CHARACTERIZING CONTROL-PATH QUBITS ENTANGLEMENT

Ideally, the incoming data qubit $|\psi\rangle_s$ frequency encoded in a microwave pulse will be routed by a control qubit $(\cos\theta|0\rangle_c + \sin\theta e^{i\phi}|1\rangle_c)$ into the state

$$(\cos\theta|0\rangle_c |T\rangle_p + e^{i\phi} \sin\theta|1\rangle_c |R\rangle_p) |\psi\rangle_s, \tag{D1}$$

where subscripts c and s represent the control and the data qubit while $|T\rangle_p$ and $|R\rangle_p$ denote the two possible paths: transmission and reflection.

Note that for the weak coherent pulses $|\alpha\rangle$ we use, $|T\rangle_p = |\alpha\rangle_T |0\rangle_R$ and $|R\rangle_p = |0\rangle_T |\alpha\rangle_R$ are not orthogonal even in the ideal case, because $\langle 0|\alpha\rangle = \langle \alpha|0\rangle =$

$\exp(-|\alpha|^2/2) > 0$. Furthermore, the actual state of the control and the path qubits are given by Eq. (C6) due to the finite extinction ratio of the cavities, which corresponds to a leakage error outside the subspace spanned by the ideal $|T\rangle_p$ and $|R\rangle_p$ states. Therefore, the traditional methods to characterize two-qubit entanglement in the 2×2 Hilbert space such as quantum-state tomography and entanglement fidelity cannot be directly apply here. Our strategy is first to estimate this leakage error using the quantum states

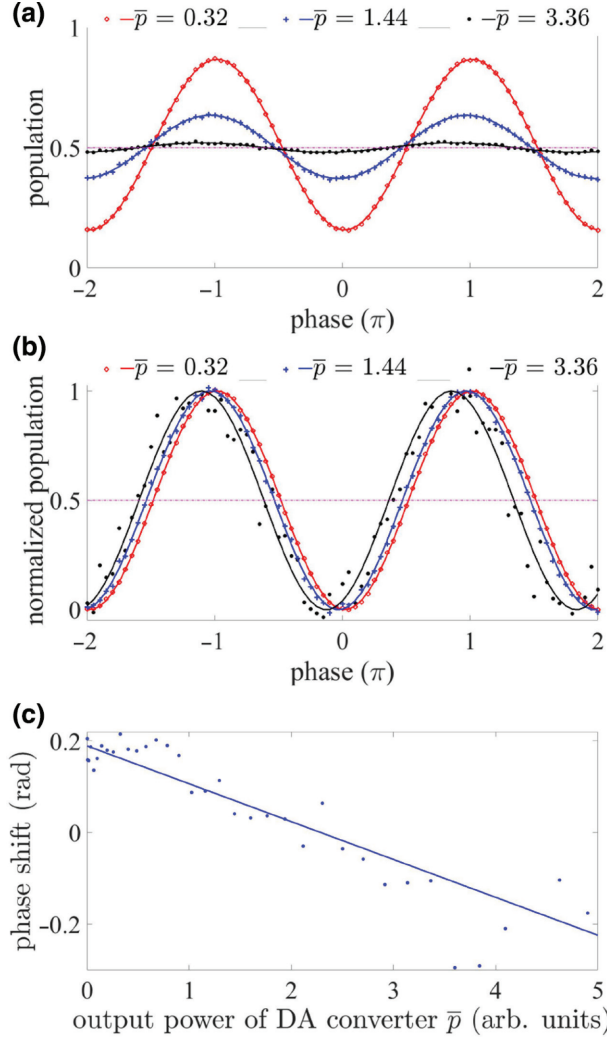


FIG. 6. Calibration of average photon number through correlation measurement. (a) The measured control qubit population in the $|+\rangle_c$ state as a function of the Bloch azimuthal angle ϕ in Eq. (C8). The value of \bar{p} is read from the output power of the digital-to-analog (DA) converter with arbitrary unit. (b) The oscillations of qubit population in (a) are normalized to $[0, 1]$ for comparison. The phase of the oscillation shows clear shifts for different signal power \bar{p} . (c) The phase of the oscillation in (a),(b) as a function of the signal power \bar{p} represented by the output of the DA converter. A linear fit is used to compare the experimental result with theory for the calibration of the average photon number N .

calibrated in Appendix C. Then we study the phase coherence within a two-dimensional Hilbert space, which the system leaks into. An entanglement witness is then used to prove the existence of entanglement between the control and the path qubits, and thus the functioning of the quantum router. Finally, we present an independent calculation of entanglement fidelity by virtually projecting the system into the single-photon subspace.

1. Control-path qubits' correlation and leakage error

As we show in Appendix C, the actual quantum state between the control and the path qubits after the quantum router can be given by

$$\cos \theta |0\rangle_c |\alpha_0^T\rangle_T |\alpha_0^R\rangle_R + e^{i\phi} \sin \theta |1\rangle_c |\alpha_1^T\rangle_T |\alpha_1^R\rangle_R \quad (\text{D2})$$

due to the finite extinction ratio of the cavity. The fidelity between this state and the ideal state Eq. (D1) can then be computed. However, this may not be a good indicator for the quality of the quantum router: the fidelity goes to 1 when average photon number $N \rightarrow 0$ due to the large overlap in the vacuum component, yet we are interested in the single-photon part. Actually, since the portion of the leaked photons stay roughly the same for a weak coherent pulse independent of the average photon number, we can use the ratio of the output power on each path to represent the probability of detecting the path qubit in each mode. Specifically we have

$$\begin{aligned} P(T|0) &= \frac{|\alpha_0^T|^2}{|\alpha_0^T|^2 + |\alpha_0^R|^2} = \frac{1 - r|\gamma_R|^2}{1 - |\gamma_T|^2|\gamma_R|^2}, \\ P(R|0) &= \frac{|\alpha_0^R|^2}{|\alpha_0^T|^2 + |\alpha_0^R|^2} = \frac{|\gamma_R|^2(r - |\gamma_T|^2)}{1 - |\gamma_T|^2|\gamma_R|^2}, \\ P(T|1) &= \frac{|\alpha_1^T|^2}{|\alpha_1^T|^2 + |\alpha_1^R|^2} = \frac{|\gamma_T|^2(1 - r|\gamma_R|^2)}{r(1 - |\gamma_T|^2|\gamma_R|^2)}, \\ P(R|1) &= \frac{|\alpha_1^R|^2}{|\alpha_1^T|^2 + |\alpha_1^R|^2} = \frac{r - |\gamma_T|^2}{r(1 - |\gamma_T|^2|\gamma_R|^2)}, \end{aligned} \quad (\text{D3})$$

as the conditional probability of finding the path qubit in T or R modes when the control qubit is projected to $|0\rangle_c$ or $|1\rangle_c$.

For example, we set the input signal as the low-frequency state $|f_l\rangle$ or the high-frequency state $|f_h\rangle$ with an average photon number of 0.35. For the low-frequency component $|f_l\rangle$, we measure $\alpha_0^{TL} = 0.56$, $\alpha_0^{RL} = 0.18e^{0.98i}$, $\alpha_1^{TL} = 0.21e^{-0.72i}$, $\alpha_1^{RL} = 0.54$, and thus we obtain $P_L(T|0) = 0.91$, $P_L(R|0) = 0.09$, $P_L(T|1) = 0.13$, and $P_L(R|1) = 0.87$. For the high-frequency component we have $\alpha_0^{TH} = 0.54$, $\alpha_0^{RH} = 0.25e^{-1.17i}$, $\alpha_1^{TH} = 0.15e^{-2.65i}$, $\alpha_1^{RH} = 0.56$, accordingly we have $P_H(T|0) = 0.82$, $P_H(R|0) = 0.18$, $P_H(T|1) = 0.06$, and $P_H(R|1) = 0.94$. The derived conditional probabilities indicate strong

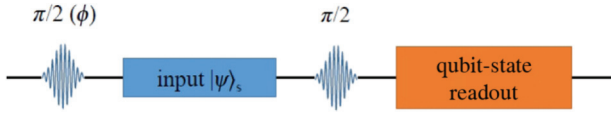


FIG. 7. Experimental pulse sequences to estimate the phase coherence and to witness the control-path entanglement. The state of the control qubit is first prepared in $|0\rangle_c + e^{i\phi}|1\rangle_c$, then the input signal is sent into the router and the output voltage from path $T - R$ is measured. The state of the control qubit is then projected onto $|\pm\rangle_c$ basis and measured in a single shot. According to state projection result of the control qubit, the measured output signal is recorded and averaged. We scan the azimuthal angle ϕ to get the oscillation curve of the output voltage, as shown in Fig. 3(a) of the main text.

correlations between the states of the control and the path qubits and thus good performance of our quantum router in the computational basis, as shown in Fig. 2 in the main text.

2. Phase coherence

Having characterized the leakage error from the ideal state, now we limit ourselves in a two-dimensional Hilbert space spanned by $|0\rangle_c |\alpha_0^T\rangle |\alpha_0^R\rangle$ and $|1\rangle_c |\alpha_1^T\rangle |\alpha_1^R\rangle$. Ideally, even with a finite extinction ratio of the cavity, we shall still get a pure state as Eq. (C6) when the control qubit is initially prepared to $(|0\rangle_c + e^{i\phi}|1\rangle_c)/\sqrt{2}$. However, we may have phase uncertainty between the two basis states. In typical qubit experiments, such a dephasing effect can be measured by a Ramsey-like experiment. Similarly, here we exploit the interference between the T and R modes.

Specifically, we measure the conditional average output amplitude, that is, a suitably normalized output voltage, in the $T - R$ mode with the control qubit being at $|+\rangle_c = (|0\rangle_c + |1\rangle_c)/\sqrt{2}$. Mathematically we can express our observable as $|+\rangle\langle +|_c \otimes a_-$.

Note that although a_- is not a Hermitian operator, the real and imaginary parts, $x = 1/2(a_-^\dagger + a_-)$ and $p = i/2(a_-^\dagger - a_-)$, can be obtained from the output voltage acquired by the homodyne detector [30,31]. To be more specified, the measured voltage can be expressed as $V = I + iQ$, where I and Q are the two quadrature amplitudes of the homodyne detection. We have

$$\langle a_- \rangle = ke^{i\theta_g} V, \quad (\text{D4})$$

where k is a scale factor and θ_g is a global phase factor introduced by the measurement setup. Therefore, once the global phase θ_g is calibrated, the real and imaginary part of $|+\rangle\langle +|_c \otimes a_-$ can be extracted from the two quadrature amplitudes of the homodyne detection, respectively. From

Eqs. (C8) and (C11) we know that the theoretical value is

$$\langle \Psi | (|+\rangle_c \langle +|_c \otimes a_-) | \Psi \rangle = P_{+A_+} = \frac{1}{4\sqrt{2}} \{ (\alpha_0^- \alpha_1^-) + \pm C[\alpha_0^- e^{-i(\phi+\delta)} + \alpha_1^- e^{i(\phi+\delta)}] \}, \quad (\text{D5})$$

where the variables are defined in Sec. 2 and can be determined when we calibrate the parameters of the quantum state.

In the experiment, we scan ϕ and measure the amplitude of the oscillation in our observable. A phase uncertainty between the two basis states can be absorbed into the uncertainty of ϕ , which will reduce the amplitude of this oscillation through $\langle \exp(i\phi') \rangle = \exp(i\phi - \sigma^2/2)$ where we assume a Gaussian random distribution $N(\phi, \sigma^2)$ for the perturbed phase ϕ' . Thus if we measure the actual oscillation amplitude of $|+\rangle\langle +|_c \otimes a_-$ and calculate its ratio with the theoretical value from the calibrated experimental parameters, we get $\exp(-\sigma^2/2)$, which is further related to the fidelity in this subspace as $F = [1 + \exp(-\sigma^2/2)]/2$.

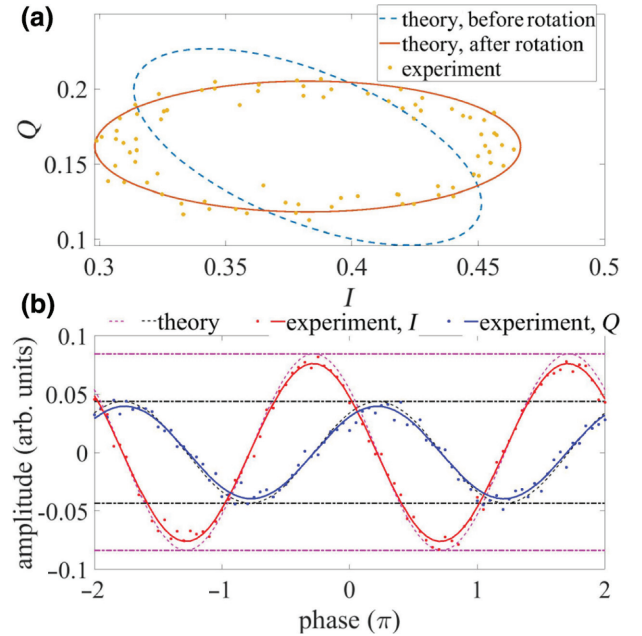


FIG. 8. Comparisons on the conditional average amplitudes obtained from the theory [Eq. (D5)] and measured in the experiment for an average photon number $\bar{n} = 2.56$. (a) The real and imaginary part of the conditional amplitudes plotted on the I/Q plane for both of the theoretical results and the experimental data. The theoretical ellipse (dashed line) is tilted to the same orientation as that of the experimental one (scattered points) by adjusting the global phase value [Eq. (D4)] of the conditional amplitude, as indicated by the solid line. (b) Oscillation of I and Q voltages as a function of ϕ . The scattered plots are experimental results, which are fitted with sine curves (solid lines). The corresponding theoretical results are plotted as dashed lines.

The experimental sequence is shown in Fig. 7. We first set the state of the control qubit in $(|0\rangle_c + e^{i\phi} |1\rangle_c)/\sqrt{2}$, then send the input signal to the router and measure the corresponding in-phase and quadrature output. The control qubit state is then projected to the $|\pm\rangle_c$ basis by a $\pi/2$ pulse followed by a strong readout pulse. The in-phase and quadrature signals from path $T-R$ is then recorded and averaged according to the qubit projection result. We further correct the control qubit dephasing between the routing process and the final measurement (see Appendix F) and the qubit readout error. In this way we obtain the four conditional output amplitudes $I(|\pm\rangle \langle \pm|_c)$ and $Q(|\pm\rangle \langle \pm|_c)$, corresponding to the signal field quadratures $x(|\pm\rangle_c)$ and $p(|\pm\rangle_c)$ in the main text, when the control qubit is projected to either $|+\rangle_c$ or $|-\rangle_c$. The complex conditional amplitudes $|+\rangle \langle +|_c \otimes a_-$ or $|-\rangle \langle -|_c \otimes a_-$ on the I/Q plane are elliptical and the measured voltages show sinusoidal oscillations as a function of ϕ , as shown in Fig. 8 and in Sec. 2.

In order to compare the measured conditional amplitudes with the theoretical ones [Eq. (D5)], we rotate the ellipse of the complex amplitude obtained from the theory to the same orientation as that of the experimental data, as illustrated in Fig. 8(a), by adjusting the global phase term [in Eq. (D4)] of the complex amplitude. Then we can directly compare the four measured voltage oscillations, $I(|\pm\rangle \langle \pm|_c)$ and $Q(|\pm\rangle \langle \pm|_c)$, to the corresponding theoretical ones to calculate fidelity from the theoretical state, as shown in Figs. 8(b) and 3(b) in the main text. Therefore, for a certain input quantum state with a given photon number, one would have four fidelity values from the experiments. We take the averaged value as the final fidelity and the maximum and minimum values as the error bars. A typical result for an average photon number of 0.4 is shown

in Fig. 3(a) in the main text. For this measurement we get $F = 0.95 \pm 0.02$.

3. Entanglement witness

As we mention in the beginning of this section, the states of the two paths $|T\rangle_p$ and $|R\rangle_p$ are not orthogonal, and thus the output state is not maximally entangled even in the ideal case. In this subsection we construct an entanglement witness W to prove the control-path qubits entanglement between the control qubit and the paths.

For an entanglement witness W , all separable states ρ_{sep} meet $\text{Tr}(\rho_{\text{sep}}W) \geq 0$. Conversely, $\text{Tr}(\rho W) < 0$ indicates the existence of quantum entanglement in the state ρ [17]. In our experiment, we construct an entanglement witness $W = \beta I - |\psi\rangle \langle \psi|$ with $|\psi\rangle = (|0\rangle_c |\alpha_0^T\rangle_T |\alpha_0^R\rangle_R + |1\rangle_c |\alpha_1^T\rangle_T |\alpha_1^R\rangle_R)/\sqrt{2}$, the theoretical output state after the routing under finite extinction ratio. Clearly the second term in the entanglement witness gives the fidelity we measure in Sec. 2. The value of β needs to be chosen such that all the product states produce a non-negative witness. According to Ref. [18], it is given by the square of the largest Schmidt coefficient of $|\psi\rangle$, i.e., the largest eigenvalue of

$$\begin{aligned} \rho_c &= \text{Tr}_p(|\psi\rangle \langle \psi|) \\ &= \frac{1}{2} \left(|0\rangle_c \langle 0|_c + |1\rangle_c \langle 1|_c + \langle \alpha_1^T | \alpha_0^T \rangle \langle \alpha_1^R | \alpha_0^R \rangle |0\rangle_c \langle 1|_c \right. \\ &\quad \left. + \langle \alpha_0^T | \alpha_1^T \rangle \langle \alpha_0^R | \alpha_1^R \rangle |1\rangle_c \langle 0|_c \right), \end{aligned} \quad (\text{D6})$$

where Tr_p represents partial trace over the paths.

Solving the eigenvalue and plugging the expressions in Eq. (C15), we have

$$\begin{aligned} \beta &= \frac{1 + |\langle \alpha_0^R | \alpha_1^R \rangle| \times |\langle \alpha_0^T | \alpha_1^T \rangle|}{2} \\ &= \frac{1}{2} \left(1 + \exp \left\{ \left[-\frac{1+r}{2} + \frac{\text{Re}(\gamma_T)(1-r|\gamma_R|^2) + \text{Re}(\gamma_R)(r-|\gamma_T|^2)}{1-|\gamma_R|^2|\gamma_T|^2} \right] N \right\} \right), \end{aligned} \quad (\text{D7})$$

which is determined by the calibrated experimental parameters. We test the existence of entanglement in various conditions, as shown in Fig. 3(b) of the main text.

4. Control-path entanglement fidelity by virtual single-photon projection

If we hypothetically project the control-path quantum state [Eq. (C6)] into the single-photon subspace, we get

$$\begin{aligned} &\frac{1}{\sqrt{2}} \left[|0\rangle_c \left(\alpha_0^T a_T^\dagger \alpha_0^R a_R^\dagger \right) |0\rangle \right. \\ &\quad \left. + e^{i\delta\phi} |1\rangle_c \left(\alpha_1^T a_T^\dagger + \alpha_1^R a_R^\dagger \right) |0\rangle \right] \end{aligned} \quad (\text{D8})$$

with suitable normalization. We express the phase noise $\delta\phi$ explicitly, which follows a Gaussian distribution with variance σ^2 . From this state we can compute the entanglement fidelity, i.e., the fidelity with the maximally entangled state

$(|0\rangle_c a_T^\dagger |0\rangle + |1\rangle_c a_R^\dagger |0\rangle)/\sqrt{2}$. For an average input photon number of 0.4 we get $\bar{F} = 0.865$, which is larger than the entanglement threshold of 0.5.

APPENDIX E: COMPUTING PROCESS FIDELITY OF ROUTED DATA QUBIT

From the error model we develop in Appendix C, if we send a weak coherent pulse with both low- and high-frequency components $|\alpha_L\rangle_L |\alpha_H\rangle_H$ through the quantum router when the control qubit is in $\cos\theta |0\rangle_c +$

$e^{i\phi} \sin\theta |1\rangle_c$, the output state will be

$$|\Psi\rangle = \cos\theta |0\rangle_c |\alpha_0^{TL}\rangle_{TL} |\alpha_0^{TH}\rangle_{TH} |\alpha_0^{RL}\rangle_{RL} |\alpha_0^{RH}\rangle_{RH} + e^{i\phi} \sin\theta |1\rangle_c |\alpha_1^{TL}\rangle_{TL} |\alpha_1^{TH}\rangle_{TH} |\alpha_1^{RL}\rangle_{RL} |\alpha_1^{RH}\rangle_{RH}. \quad (\text{E1})$$

There can be an additional phase noise in the superposition state, which mainly comes from the dephasing of the control qubit. This will not be a problem since this phase acts on the low- and high-frequency components in the same way.

Let us virtually project the quantum state to the single-photon subspace Π_1 :

$$\begin{aligned} \Pi_1 |\Psi\rangle = & \cos\theta |0\rangle_c \left(\alpha_0^{TL} a_{TL}^\dagger + \alpha_0^{TH} a_{TH}^\dagger + \alpha_0^{RL} a_{RL}^\dagger + \alpha_0^{RH} a_{RH}^\dagger \right) |0\rangle \\ & + e^{i\phi} \sin\theta |1\rangle_c \left(\alpha_1^{TL} a_{TL}^\dagger + \alpha_1^{TH} a_{TH}^\dagger + \alpha_1^{RL} a_{RL}^\dagger + \alpha_1^{RH} a_{RH}^\dagger \right) |0\rangle. \end{aligned} \quad (\text{E2})$$

For an ideal quantum router we have $\alpha_0^{TL} = \alpha_L$, $\alpha_0^{RL} = 0$, $\alpha_0^{TH} = \alpha_H$, $\alpha_0^{RH} = 0$, $\alpha_1^{TL} = \alpha_L$, $\alpha_1^{RL} = 0$, $\alpha_1^{TH} = \alpha_H$, $\alpha_1^{RH} = 0$, thus the input data qubit $(\alpha_L a_L^\dagger + \alpha_H a_H^\dagger) |0\rangle$ (with suitable normalization) is well preserved for both T and R paths.

For the actual performance of the quantum router, we calibrate from Eq. (C15)

$$\begin{aligned} \alpha_0^{T,L(H)} &= \alpha_{L(H)} \sqrt{\frac{1 - r_{L(H)} |\gamma_{R,L(H)}|^2}{1 - |\gamma_{T,L(H)} \gamma_{R,L(H)}|^2}}, \\ \alpha_1^{T,L(H)} &= \gamma_{T,L(H)} \alpha_{L(H)} \sqrt{\frac{1 - r_{L(H)} |\gamma_{R,L(H)}|^2}{1 - |\gamma_{T,L(H)} \gamma_{R,L(H)}|^2}}, \\ \alpha_0^{R,L(H)} &= \gamma_{R,L(H)} \alpha_{L(H)} \sqrt{\frac{r_{L(H)} - |\gamma_{T,L(H)}|^2}{1 - |\gamma_{T,L(H)} \gamma_{R,L(H)}|^2}}, \\ \alpha_1^{R,L(H)} &= \alpha_{L(H)} \sqrt{\frac{r_{L(H)} - |\gamma_{T,L(H)}|^2}{1 - |\gamma_{T,L(H)} \gamma_{R,L(H)}|^2}}, \end{aligned} \quad (\text{E3})$$

where the additional index L (H) represents the parameters measured for the low- (high-) frequency component. This allows us to study the deviation from the identity channel in the data qubit subspace both for the transmitted and the reflected paths.

In principle, an analytical expression for the actual quantum channel can be derived, which however can be very complicated. Here instead we plug in the calibrated experimental parameters and perform numerical calculation for quantum-process tomography [19]. For each routed path, the transformation in the data qubit subspace can be

described by a quantum channel $\rho \rightarrow \sum_{mn} E_m \rho E_n^\dagger \eta_{mn}$, where $\{E_m\}$ represents a fixed set of basis operators used to

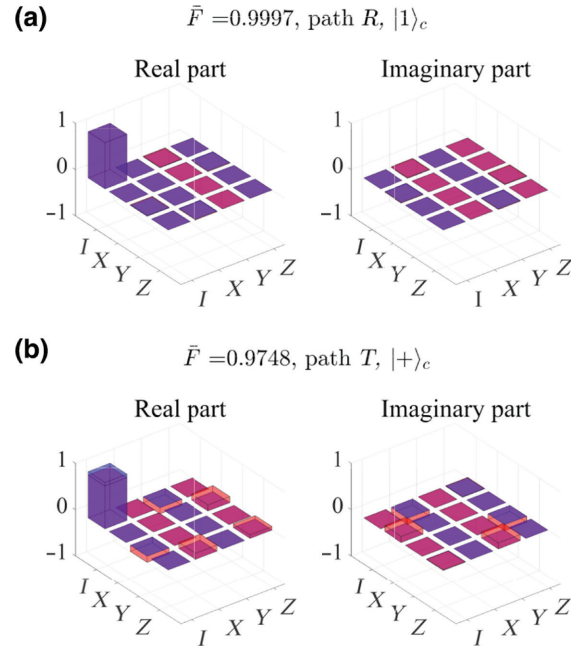


FIG. 9. Real and imaginary parts of the reconstructed process matrices by setting the control qubit in (a) $|1\rangle_c$ state and (b) $|+\rangle_c = (|0\rangle_c + |1\rangle_c)/\sqrt{2}$ state. The routed signal is recorded on (a) the reflection path R and (b) the transmission path T . The corresponding matrix elements for an ideal routing operation are indicated with the blue hollow caps. The corresponding average gate fidelity \bar{F} are also labeled.

expand the final state and η_{mn} represents the element of a process matrix η . For the single-qubit process tomography, we use the basis operators as $I = I$, $X = \sigma_x$, $Y = -i\sigma_y$, $Z = \sigma_z$, which requires the measurements on four different initial states (a) $\alpha_L = 1$, $\alpha_H = 0$, (b) $\alpha_L = 0$, $\alpha_H = 1$, (c) $\alpha_L = 1$, $\alpha_H = 1$, and (d) $\alpha_L = 1$, $\alpha_H = -i$. Note that in the experiment we need to consider the small photon number limit $|\alpha_L|^2, |\alpha_H|^2 \ll 1$, but once we obtain Eq. (E3), only the relative amplitudes matter and we can arbitrarily scale α_L and α_H for convenience.

First we set the state of the control qubit to $(|0\rangle_c + |1\rangle_c)/\sqrt{2}$ and choose the input data qubit to be one of the four aforementioned states. For each input state we compute the output state on the path R using Eq. (E3) and get the corresponding density matrix after normalization. Then we can reconstruct the experimental process matrix η_e and compare it with the ideal one η_{id} to calculate the process fidelity $F_p = \text{tr}(\eta_e \eta_{id})$. According to Ref. [20] the average gate fidelity \bar{F} can be calculated through $\bar{F} = (dF_p + 1)/(d + 1)$, where $d = 2$ is the dimension of the concerned Hilbert space. The result is shown in Fig. 4 of the main text.

In order to have a comprehensive evaluation of the routing process, this process tomography is carried out with different states of the control qubit and different output paths. In Fig. 9(a), we show the reconstructed process matrix by setting the control qubit to $|1\rangle_c$ and recording the output signal at path R . In Fig. 9(b), we set the control qubit to $(|0\rangle_c + |1\rangle_c)/\sqrt{2}$ and consider the output signal from path T . Both of them show high fidelities of better than 97%, which indicates that the input quantum state can be well preserved during the routing operation. Benefiting from our frequency-encoding scheme, the quantum state of the data qubit is robust to absolute leakage error of the low-frequency and high-frequency components between paths T and R , but only sensitive to the asymmetric response at the two frequencies.

APPENDIX F: CORRECTION DUE TO CONTROL QUBIT DECOHERENCE

Due to a delay between the routing of the quantum signal and the measurement of the control qubit, and the finite coherence time T_2 of the control qubit (as shown in Table I), the final state we obtain will be different from the output state of the quantum router. In particular, when measuring the conditional output voltage, the control qubit states $|\pm\rangle_c$ may be exchanged because of the phase error. Let us denote the probability of measuring the control qubit in $|\pm\rangle_c$ at time delay t by $P_{\pm}(t)$. For an interval $t_0 = 2 \mu\text{s}$ between the routing process and the measurement, we have $P_{\pm}(t = t_0) = \{1 \pm [P_+(t = 0) - P_-(t = 0)] \exp(-t_0/T_2)\}/2$, and the average amplitudes we measured are $P_{\pm}(t = t_0)A_{\pm}(t = t_0) = \{[1 + \exp(-t_0/T_2)]P_{\pm}(t = 0)A_{\pm}(t = 0) + [1 - \exp(-t_0/T_2)]P_{\mp}(t = 0)A_{\mp}(t = 0)\}/2$.

$(t = 0)A_{\mp}(t = 0)\}/2$. By solving these equations, we can correct the conditional average amplitudes $P_{\pm}(t = 0)A_{\pm}(t = 0) = \{[1 + \exp(t_0/T_2)]P_{\pm}(t = t_0)A_{\pm}(t = t_0) + [1 - \exp(t_0/T_2)]P_{\mp}(t = t_0)A_{\mp}(t = t_0)\}/2$.

-
- [1] K. Lemr, K. Bartkiewicz, A. Černoč, and J. Soubusta, Resource-efficient linear-optical quantum router, *Phys. Rev. A* **87**, 062333 (2013).
 - [2] X. X. Yuan, J. J. Ma, P. Y. Hou, X. Y. Chang, C. Zu, and L. M. Duan, Experimental demonstration of a quantum router, *Sci. Rep.* **5**, 12452 (2015).
 - [3] K. Bartkiewicz, A. Černoč, and K. Lemr, Implementation of an efficient linear-optical quantum router, *Sci. Rep.* **8**, 13480 (2018).
 - [4] H. J. Kimble, The quantum internet, *Nature* **453**, 1023 (2008).
 - [5] V. Giovannetti, S. Lloyd, and L. Maccone, Quantum Random Access Memory, *Phys. Rev. Lett.* **100**, 160501 (2008).
 - [6] A. W. Harrow, A. Hassidim, and S. Lloyd, Quantum Algorithm for Linear Systems of Equations, *Phys. Rev. Lett.* **103**, 150502 (2009).
 - [7] P. Reberstrost, M. Mohseni, and S. Lloyd, Quantum Support Vector Machine for big Data Classification, *Phys. Rev. Lett.* **113**, 130503 (2014).
 - [8] S. Lloyd, M. Mohseni, and P. Reberstrost, Quantum principal component analysis, *Nat. Phys.* **10**, 631 (2014).
 - [9] J. Biamonte, P. Wittek, N. Pancotti, P. Reberstrost, N. Wiebe, and S. Lloyd, Quantum machine learning, *Nature* **549**, 195 (2017).
 - [10] V. Giovannetti, S. Lloyd, and L. Maccone, Architectures for a quantum random access memory, *Phys. Rev. A* **78**, 052310 (2008).
 - [11] A. Sala and M. Blaauboer, Proposal for a transmon-based quantum router, *Journal of Physics: Condensed Matter* **28**, 275701 (2016).
 - [12] C. T. Hann, C.-L. Zou, Y. Zhang, Y. Chu, R. J. Schoelkopf, S. M. Girvin, and L. Jiang, Hardware-Efficient Quantum Random Access Memory with Hybrid Quantum Acoustic Systems, *Phys. Rev. Lett.* **123**, 250501 (2019).
 - [13] A. Blais, R.-S. Huang, A. Wallraff, S. M. Girvin, and R. J. Schoelkopf, Cavity quantum electrodynamics for superconducting electrical circuits: An architecture for quantum computation, *Phys. Rev. A* **69**, 062320 (2004).
 - [14] L.-M. Duan and H. J. Kimble, Scalable Photonic Quantum Computation through Cavity-Assisted Interactions, *Phys. Rev. Lett.* **92**, 127902 (2004).
 - [15] J. M. Lukens and P. Lougovski, Frequency-encoded photonic qubits for scalable quantum information processing, *Optica* **4**, 8 (2017).
 - [16] I.-C. Hoi, C. M. Wilson, G. Johansson, T. Palomaki, B. Peropadre, and P. Delsing, Demonstration of a Single-Photon Router in the Microwave Regime, *Phys. Rev. Lett.* **107**, 073601 (2011).
 - [17] M. Lewenstein, B. Kraus, J. I. Cirac, and P. Horodecki, Optimization of entanglement witnesses, *Phys. Rev. A* **62**, 052310 (2000).
 - [18] M. Bourennane, M. Eibl, C. Kurtsiefer, S. Gaertner, H. Weinfurter, O. Gühne, P. Hyllus, D. Bruß, M. Lewenstein,

- and A. Sanpera, Experimental Detection of Multipartite Entanglement Using Witness Operators, *Phys. Rev. Lett.* **92**, 087902 (2004).
- [19] M. A. Nielsen and I. L. Chuang, *Quantum Computation and Quantum Information* (Cambridge University Press, New York, NY, United States, 2000).
- [20] A. G. White, A. Gilchrist, G. J. Pryde, J. L. O'Brien, M. J. Bremner, and N. K. Langford, Measuring two-qubit gates, *J. Opt. Soc. Am. B.* **24**, 172 (2007).
- [21] Z. H. Peng, S. E. de Graaf, J. S. Tsai, and O. V. Astafiev, Tuneable on-demand single-photon source in the microwave range, *Nat. Commun.* **7**, 12588 (2016).
- [22] P. Forn-Díaz, C. W. Warren, C. W. S. Chang, A. M. Vadiraj, and C. M. Wilson, On-Demand Microwave Generator of Shaped Single Photons, *Phys. Rev. Appl.* **8**, 054015 (2017).
- [23] K. Inomata, Z. Lin, K. Koshino, W. D. Oliver, J.-S. Tsai, T. Yamamoto, and Y. Nakamura, Single microwave-photon detector using an artificial λ -type three-level system, *Nat. Commun.* **7**, 12303 (2016).
- [24] S. Kono, K. Koshino, Y. Tabuchi, A. Noguchi, and Y. Nakamura, Quantum non-demolition detection of an itinerant microwave photon, *Nat. Phys.* **14**, 546 (2018).
- [25] J.-C. Besse, S. Gasparinetti, M. C. Collodo, T. Walter, P. Kurpiers, M. Pechal, C. Eichler, and A. Wallraff, Single-Shot Quantum Nondemolition Detection of Individual Itinerant Microwave Photons, *Phys. Rev. X* **8**, 021003 (2018).
- [26] W.-B. Yan and H. Fan, Single-photon quantum router with multiple output ports, *Sci. Rep.* **4**, 4820 (2014).
- [27] B. J. Chapman, E. I. Rosenthal, J. Kerckhoff, B. A. Moores, L. R. Vale, J. A. B. Mates, G. C. Hilton, K. Lalumière, A. Blais, and K. W. Lehnert, Widely Tunable On-Chip Microwave Circulator for Superconducting Quantum Circuits, *Phys. Rev. X* **7**, 041043 (2017).
- [28] P. Eder, T. Ramos, J. Goetz, M. Fischer, S. Pogorzalek, J. P. Martínez, E. P. Menzel, F. Loacker, E. Xie, J. J. Garcia-Ripoll, K. G. Fedorov, A. Marx, F. Deppe, and R. Gross, Quantum probe of an on-chip broadband interferometer for quantum microwave photonics, *Superconductor Science and Technology* **31**, 115002 (2018).
- [29] J. Gao and J. Zmuidzinas, C. I. o. T. D. of Engineering, and A. Science, *The Physics of Superconducting Microwave Resonators* (California Institute of Technology, Pasadena, CA, United States, 2008).
- [30] M. P. da Silva, D. Bozyigit, A. Wallraff, and A. Blais, Schemes for the observation of photon correlation functions in circuit qed with linear detectors, *Phys. Rev. A* **82**, 043804 (2010).
- [31] C. Eichler, D. Bozyigit, and A. Wallraff, Characterizing quantum microwave radiation and its entanglement with superconducting qubits using linear detectors, *Phys. Rev. A* **86**, 032106 (2012).